

# ELUCID-DESI I: A Parallel MPI Implementation of the Initial Condition Solver for Large-Scale Reconstruction Simulations

Wensheng Hong<sup>1,2</sup>, Xiaohu Yang<sup>1,2\*</sup>, Junde Li<sup>1,2</sup>, Huiyuan Wang<sup>3</sup>, Zhao Chen<sup>1,2</sup>, Hong-Ming Zhu<sup>4</sup>,  
Qingyang Li<sup>1,2</sup>, Yizhou Gu<sup>1,2</sup>, Youcai Zhang<sup>5</sup>, Feng Shi<sup>6</sup>, Jiaxin Han<sup>1,2</sup>, Yu Yu<sup>1,2</sup>, Zhongxu Zhai<sup>1,2</sup>

<sup>1</sup>*State Key Laboratory of Dark Matter Physics, Tsung-Dao Lee Institute & School of Physics and Astronomy, Shanghai Jiao Tong University, Shanghai 201210, China*

<sup>2</sup>*Shanghai Key Laboratory for Particle Physics and Cosmology, and Key Laboratory for Particle Physics, Astrophysics and Cosmology, Ministry of Education, Shanghai Jiao Tong University, Shanghai 200240, China*

<sup>3</sup>*Key Laboratory for Research in Galaxies and Cosmology, Department of Astronomy, University of Science and Technology of China, Hefei, Anhui 230026, China*

<sup>4</sup>*National Astronomical Observatories, Chinese Academy of Sciences, 20A Datun Road, Beijing 100101, China*

<sup>5</sup>*Shanghai Astronomical Observatory, Nandan Road 80, Shanghai 200030, China*

<sup>6</sup>*School of Aerospace Science And Technology, Xidian University, Xi'an 710126, China*

Accepted XXX. Received YYY; in original form ZZZ

## ABSTRACT

We present a highly scalable, MPI-parallelized framework for reconstructing the initial cosmic density field, designed to meet the computational demands of next-generation cosmological simulations, particularly the upcoming ELUCID-DESI simulation based on DESI BGS data. Building upon the Hamiltonian Monte Carlo approach and the FastPM solver, our code employs domain decomposition to efficiently distribute memory between nodes. Although communication overhead increases the per-step runtime of the MPI version by roughly a factor of eight relative to the shared-memory implementation, our scaling tests—spanning different particle numbers, core counts, and node layouts—show nearly linear scaling with respect to both the number of particles and the number of CPU cores. Furthermore, to significantly reduce computational costs during the initial burn-in phase, we introduce a novel “guess” module that rapidly generates a high-quality initial density field. The results of the simulation test confirm substantial efficiency gains: for  $256^3$  particles, 53 steps ( $\sim 54$  CPU hours) are saved; for  $1024^3$ , 106 steps ( $\sim 7500$  CPU hours). The relative gain grows with the number of particles, rendering large-volume reconstructions computationally practical for upcoming surveys, including our planned ELUCID-DESI reconstruction simulation with  $8192^3$  particles, with a rough estimation of 720 steps ( $\sim 37,000,000$  CPU hours).

**Key words:** dark matter – galaxies: halos – large-scale structure of universe – methods: statistical

## 1 INTRODUCTION

We are entering a new era of observations powered by fourth-generation wide-field spectroscopic surveys. The Dark Energy Spectroscopic Instrument (DESI Collaboration et al. 2016a,b), the Prime Focus Spectrograph (Takada et al. 2014), the Chinese Space Station Survey Telescope (Zhan 2011; Gong et al. 2019; CSST Collaboration et al. 2025), and the Jiao-tong University Spectroscopic Telescope (JUST Team et al. 2024) will collectively map hundreds of millions of galaxies over cosmological volumes that exceed those of earlier surveys by roughly an order of magnitude. In addition to their central objectives of probing the nature of dark energy and the properties of dark matter, these surveys will provide a powerful resource for studying how galaxies with a wide range of characteristics form and evolve in concert with the build-up of cosmic dark matter structures (Mo et al. 2010).

To understand how galaxies assemble throughout the cosmic density field, it is essential to investigate the spatial distributions and internal characteristics of both galaxies and the intergalactic medium

(IGM), as well as their mutual interactions, within dark matter halos that cover a wide range of masses and reside in varied environments of the cosmic web. Traditionally, constraints on models of galaxy formation have largely come from statistical comparisons (e.g., Kauffmann et al. 1993; Guo et al. 2011), assessing how well theoretical predictions match key observables such as the galaxy luminosity and stellar mass functions, galaxy clustering (e.g., Zehavi et al. 2005, 2011; Yang et al. 2012), halo occupation statistics (e.g., Jing et al. 1998; Zheng et al. 2005), and the conditional luminosity and stellar mass functions (e.g., Yang et al. 2008, 2009; Wang et al. 2024b). Yet, because galaxy formation involves highly complex and intertwined physical processes, these statistical approaches have not fully exploited the richness of observational data, as many processes remain effectively decoupled in such analyses. A particularly powerful way to harness observational information is through constrained simulations, in which the initial density field is directly inferred from observations. This approach enables detailed, object-by-object comparisons and thus provides a more stringent means of constraining galaxy formation physics.

In this context, considerable work has gone into developing methods to infer the initial conditions of structure formation in the nearby

\* xyang@sjtu.edu.cn

Universe from galaxy surveys and/or measurements of peculiar velocities (Sousa et al. 2007; Jasche & Wandelt 2013; Seljak et al. 2017). Hoffman & Ribak (1991) presented a method for generating Gaussian random fields that satisfy an imposed set of constraints (see also Bertschinger 1987; van de Weygaert & Bertschinger 1996; Kitaura & Enßlin 2008). The measured peculiar motions of galaxies in the local volume have similarly been widely employed to set up initial conditions for constrained simulations (e.g., Kravtsov et al. 2002; Klypin et al. 2003; Doumler et al. 2013). Alongside these backward-modeling approaches, Hamiltonian Markov Chain Monte Carlo (HMC) reconstruction techniques have been steadily improved and extended (Jasche & Wandelt 2013; Kitaura 2013; Wang et al. 2013, 2014).

Within this family of forward-modeling approaches, the particle-mesh (PM)-based HMC framework developed by Wang et al. (2013, 2014) currently delivers the most accurate reconstructions, primarily because PM itself is a mature and well-tested simulation technique. In this approach, the negative log-posterior is treated as the potential energy of a Hamiltonian system, enabling HMC to efficiently probe the extremely high-dimensional parameter space characterizing the initial density field. Each HMC step entails the evaluation of the likelihood gradient, which in practice is equivalent to executing a full cosmological simulation. This rigorous combination of statistical mechanics with cosmological dynamics has established a new standard for statistically robust, full-volume reconstruction methodologies.

Using the group catalogs (Yang et al. 2007) constructed from the Sloan Digital Sky Survey (SDSS, York et al. 2000) main galaxy sample DR7 and the associated value-added galaxy catalogs (Blanton et al. 2005), we performed the ELUCID (Exploring the Local Universe with reConstructed Initial Density field) simulations (e.g. Wang et al. 2014; Tweed et al. 2017; Wang et al. 2016). These simulations enable us to build a one-to-one correspondence between observed galaxies and dark matter subhalos within the simulated volume (e.g. Yang et al. 2018). With this mapping in hand, we can examine how the morphology and orientation of observed galaxies are affected by the assembly histories of their host (sub)halos and by their positions in the cosmic web (e.g. Zhang et al. 2021, 2022, 2025). Moreover, it provides the observational environmental framework required to quantify how galaxy formation—covering both star formation and quenching—is governed by *in situ* and *ex situ* processes (Wang et al. 2018), among other factors.

Motivated by the opportunity to carry out much larger-volume, higher-resolution re-simulations of the local universe using the upcoming DESI BGS DR3 data (e.g., Myers et al. 2023; Hahn et al. 2023), we present the ELUCID-DESI project, which extends the redshift range to  $z < 0.4$ , beyond the original ELUCID limit of  $z < 0.12$ . Realizing this objective requires, as a crucial first step, reconstructing the initial conditions of our local universe over a volume roughly 64 times larger than before. However, the remarkable strengths of the HMC framework come at the price of very high computational demands. The key bottleneck is intrinsic: each likelihood evaluation necessitates a full forward simulation. Consequently, obtaining a well-converged Markov chain for a reconstruction over such a large volume can consume hundreds of millions of CPU core-hours, rendering routine use impractical. Furthermore, the original ELUCID configuration, like other HMC-based approaches, relies on shared-memory (OpenMP) parallelization. This architecture enforces a strict memory ceiling, since the entire problem must reside in the RAM of a single compute node—an especially restrictive limitation given the scale of upcoming datasets.

As the first paper in the ELUCID-DESI series, this work repre-

sents a step toward overcoming these challenges. We present a next-generation, massively parallel implementation of the Bayesian framework for reconstructing initial conditions. Our scheme preserves the rigorous HMC formulation of Wang et al. (2014), but is fundamentally re-engineered to confront both memory and computational-throughput limitations in giga- and tera-particle regimes. Our main advances are: (I) A distributed-memory, MPI-parallel implementation employing 3D domain decomposition, built upon the scalable FastPM particle-mesh solver. This removes the single-node memory bottleneck and enables reconstructions at scales that were previously unattainable. (II) A new intelligent initialization module that generates a high-quality initial density field proposal via a fast approximate inversion. By doing so, it directly mitigates and substantially shortens the usually prolonged burn-in phase of the HMC sampler, yielding order-of-magnitude savings in computational cost.

The remainder of the paper is organized as follows. Section 2 describes our methodology, including the HMC formalism, the parallelization approach, and the new proposal-generation module. Section 3 provides an extensive performance evaluation, including strong and weak scaling, memory usage, and validation of reconstruction fidelity relative to simulations. In Section 4, we discuss the broader implications of our results and outline prospective avenues for future work.

## 2 AN MPI CODE FOR ELUCID-DESI

This work implements and extends the Bayesian reconstruction framework to obtain the initial condition of the structure formation of the local Universe based on the density field extracted from observation using the Hamiltonian Markov Chain Monte Carlo (HMC) method, developed by Wang et al. (2013, 2014). The core idea is to sample the posterior distribution of the initial density field,  $\delta_i$ , conditioned on the observed final density field,  $\delta_f$ , by constructing a Hamiltonian system in which the potential energy is defined as the negative log-posterior.

We direct the readers to Wang et al. (2013, 2014) for a complete derivation of the Hamiltonian equations and the sampling algorithm. The focus of this section is to present our key computational advancements in this framework. Specifically, we will detail the following:

1. The overall reconstruction pipeline, highlighting the integration of the forward model and the sampler.
2. The theoretical Basic, introducing the Hamiltonian Markov Chain Monte Carlo (HMC) method.
3. The particle-mesh (PM) N-body solver, which serves as the forward model to evolve the density field and compute the likelihood gradient—the primary computational kernel.
4. A novel initial density field guess module, designed to significantly reduce the Markov chain’s burn-in period.

These components form the foundation of our new, scalable MPI-parallel reconstruction code.

### 2.1 The flowchart

Our new reconstruction code is built upon the scalable FastPM scheme, a highly efficient approximate N-body solver. We have extensively modified and extended this framework to implement the Hamiltonian Markov Chain Monte Carlo (HMC) sampler required for Bayesian reconstruction of the initial density field.

The general workflow of the reconstruction pipeline is illustrated in Figure 1. It can be logically divided into two major phases: (1) a pre-processing stage (the two blue boxes on the left side of the figure)

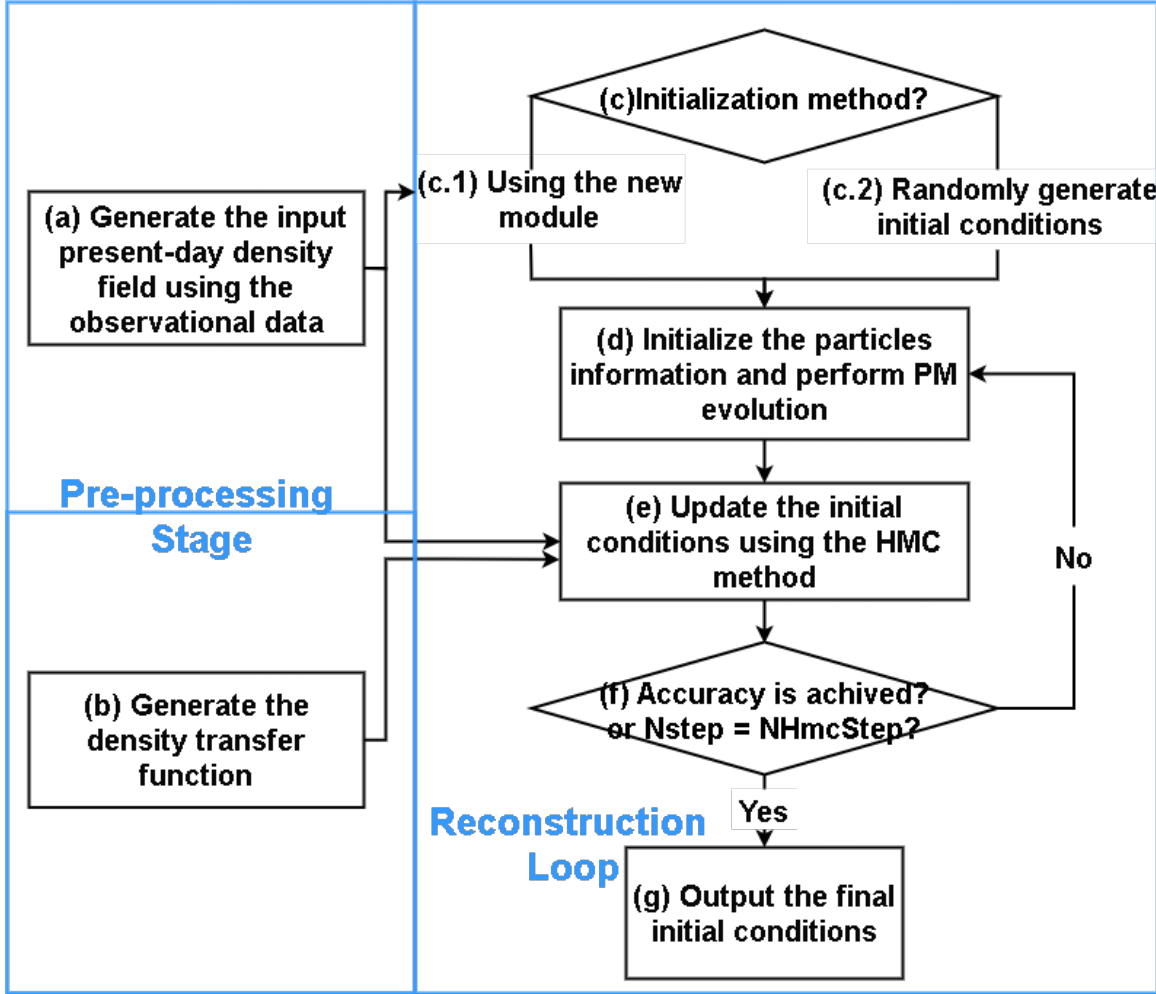


**Figure 1.** Schematic overview of the reconstruction pipeline. The workflow consists of two main stages. **Left panel:** Pre-processing stage, which prepares the necessary inputs: (a) reconstruction of the three-dimensional observed density field from survey data, and (b) calibration of the transfer function  $T(k)$  to correct for inaccuracies in the fast particle-mesh forward model. **Right panel:** The core HMC sampling stage, which iteratively samples the initial density field. The process begins by (c) generating an initial condition guess—either (c.1) randomly or (c.2) via our novel *guess module*—then (d) evolves it forward in time using the particle-mesh solver. Then, (e) the code evaluates the likelihood by comparing the predicted final field with the observed input, and updates the initial conditions via Hamiltonian dynamics. (f) This loop repeats until a predefined number of samples are collected or a required reconstruction accuracy is achieved. (g) The final reconstructed initial density field is outputted for subsequent studies.

and (2) the core HMC sampling stage (the blue box on the right side).

### 2.1.1 Pre-processing Stage: Construction of Inputs

This stage prepares two essential inputs for the reconstruction code.

- **The Present-Day Density Field,  $\rho_{\text{obs}}$  (Figure 1(a)):**

The target final density field shall be reconstructed from observational galaxy survey data. As this study mainly focuses on developing a highly efficient MPI code for the initial condition reconstruction, we will directly make use of the density field from a given N-body simulation. Observationally, we are constructing the mass, tidal tensor and velocity field from the DESI BGS data in a separate work (Li et al. 2026, in preparation). The procedures for obtaining the density field are described as follows:

- (i) Identify galaxy groups from the survey data to serve as tracers

of dark matter halos (e.g., using the group finder described in Yang et al. (2005); Yang et al. (2007)).

- (ii) Apply a mass threshold to select a robust halo sample.
- (iii) Reconstruct the continuous three-dimensional matter density field from the spatial distribution of these halos (e.g. following the techniques validated in Wang et al. (2009); Wang et al. (2012)).
- (iv) Based on the matter density field, we obtain the velocity field using linear theory.
- (v) Move groups/halos to the real space according to the velocity field.
- (vi) Iteratively obtain the final matter density field.

The resulting density field,  $\rho_{\text{obs}}$ , serves as the constraining data  $\delta_f$  for the HMC likelihood.

- **The Density Transfer Function,  $T(k)$  (Figure 1(b)):**

To bridge the accuracy gap between the FastPM approximation and a full N-body simulation, we employ a transfer function  $T(k)$ . It is computed from a pair of simulations (one based on PM evolution, one

based on standard simulation) that share the same initial conditions:

$$T(k) = \frac{\langle \rho_{N,c}(\mathbf{k}) \rho_{si}^*(\mathbf{k}) \rangle_{\mathbf{k}}}{\langle \rho_{N,c}(\mathbf{k}) \rho_{N,c}^*(\mathbf{k}) \rangle_{\mathbf{k}}}. \quad (1)$$

Here,  $\rho_{N,c}$  is the final density field obtained by cloud-in-cell (CIC) assignment after  $N_{\text{PM}}$  FastPM steps (using the code's internal particle-mesh solver), and  $\rho_{si}$  is the corresponding density field at  $z = 0$  from a high-accuracy reference simulation. This correction function is applied to the model-predicted density  $\rho_{\text{mod}}$  field during sampling:

$$\rho_{\text{mod}}(\mathbf{k}) = \frac{w_g(R_s k) T(k)}{w_c(\mathbf{k}) N_c^3} \sum_x \rho_{N,c}(\mathbf{x}) e^{-i\mathbf{k} \cdot \mathbf{x}} \quad (2)$$

where  $w_c$  is the CIC assignment kernel,  $w_g(R_s k)$  is a Gaussian smoothing kernel with scale  $R_s$  (introduced to suppress shot noise in the Hamiltonian force calculation), and  $N_c$  denotes the number of grids in one dimension.

These pre-processed inputs—the transfer function  $T(k)$  and the target density field—are then supplied to the main reconstruction loop, which carries out the HMCMC sampling to infer the posterior distribution of the initial conditions  $\delta_i$ .

### 2.1.2 Core HMCMC Sampling Stage: Reconstruction Loop

The blue box on the right side of Figure 1 highlights the main reconstruction loop, which carries out iterative Bayesian sampling using the HMCMC algorithm. The procedure unfolds as follows:

- **Initial Condition Generation (Figure 1(c)):**

The reconstruction begins by generating the initial guess  $\delta_i$  for the initial density field. Our implementation provides two distinct initialization strategies:

(i) **Conventional Random Initialization (Figure 1(c.1)):** Following standard practice, the chain starts from a random Gaussian realization consistent with the theoretical power spectrum  $P(k)$ .

(ii) **Intelligent Initial Guess (Novel) (Figure 1(c.2)):** Utilizing our newly developed *initial guess module*, which generates a physically-informed initial proposal through fast, approximate reconstruction of the input density field  $\rho_{\text{obs}}$ . This approach significantly accelerates convergence by initializing the chain near the high-probability region of the posterior distribution.

- **Forward Model Evaluation (Figure 1(d)):**

The proposed initial field  $\delta_i$  is evolved to the target redshift (typically  $z = 0$ ) using the integrated particle-mesh  $N$ -body solver. This produces a predicted final density field  $\rho_{\text{mod}}$ , which incorporates both gravitational evolution and the pre-computed correction transfer function  $T(k)$  to enhance accuracy.

- **State Update and Likelihood Computation (Figure 1(e)):**

Following the evaluation, new proposals for both the density field and momentum variables are updated via Hamiltonian dynamics:

$$\frac{d\delta_i}{dt} = \frac{\partial K}{\partial p}, \quad \frac{dp}{dt} = -\frac{\partial \psi}{\partial \delta_i}, \quad (3)$$

with numerical integration performed using a symplectic leapfrog scheme. Here,  $K$  denotes the kinetic energy of the auxiliary momentum variables and  $\psi$  represents the negative log-posterior (potential energy). This process returns to **Forward Model Evaluation** step and continues for  $N_{\text{substeps}}$  iterations.

The final predicted field  $\rho_{\text{mod}}$  is compared with the input density

field  $\rho_p$  to evaluate the Hamiltonian  $\mathcal{H}$ . The Metropolis-Hastings criterion determines whether to accept or reject the proposed state based on Hamiltonian conservation.

- **Chain Termination and Final Output (Figure 1(f,g))**

Upon completion of the pre-specified number of iterations  $N_{\text{steps}}$  or when the desired reconstruction accuracy is achieved, the Markov chain is terminated. In a full Bayesian analysis, one would retain all samples after burn-in to characterize the posterior distribution. For computational and storage efficiency in these large-scale runs, we output a single high-fidelity sample: the final accepted state  $\delta_i^{(\text{final})}$  of the chain.

We justify this choice by noting that a well-converged HMCMC chain spends the vast majority of its time in the high-probability region of the posterior. Therefore, the final state  $\delta_i^{(\text{final})}$  is effectively a sample drawn from the stationary posterior distribution and serves as a valid, high-likelihood reconstruction. It can be considered an approximation to a sample from the posterior, suitable for applications such as generating constrained simulations. For uncertainty quantification, the full chain would be required.

Optimal reconstruction efficiency requires careful tuning of several key parameters within the HMCMC framework. These include the mass assignment scheme smoothing scale  $R_s$ , the time-stepping parameters in the leapfrog integrator, and the PM force resolution. While comprehensive guidance on parameter selection is beyond the scope of this paper, users may refer to the detailed discussions and tests presented in the original ELUCID implementation papers (Wang et al. 2013, 2014) for established guidelines. Our code provides sensible defaults based on these references, but specific survey characteristics and scientific requirements may necessitate further optimization by the user.

## 2.2 Theoretical Basis: Hamiltonian Monte Carlo for Density Field Reconstruction

The goal of initial density field reconstruction is to find the initial fluctuation density field  $\delta(\mathbf{k})$  that, when evolved forward through a cosmological model, best matches an observed present-day density field  $\rho_{\text{obs}}(\mathbf{x})$ . This is formulated as a Bayesian inference problem with two fundamental constraints.

### 2.2.1 Bayesian Formulation

First, in accordance with the standard cosmological model, the initial density field is assumed to be a Gaussian random field characterized by the linear power spectrum  $P_{\text{lin}}(k)$ . Its prior probability distribution in Fourier space is:

$$P[\delta(\mathbf{k})] = \prod_{\mathbf{k}}^{\text{half}} \prod_{j=0}^1 \frac{\exp\{-[\delta_j(\mathbf{k})]^2/P_{\text{lin}}(k)\}}{[\pi P_{\text{lin}}(k)]^{1/2}}, \quad (4)$$

where the product over  $\mathbf{k}$  extends over half of Fourier space (exploiting Hermitian symmetry), and  $j = 0, 1$  index the real and imaginary components, respectively.  $P_{\text{lin}}(k)$  is the analytical linear power spectrum assuming a given set of cosmological parameters.

Second, the forward-evolved field  $\rho_{\text{mod}}(\mathbf{x})$ , obtained from  $\delta(\mathbf{k})$  through a prescribed gravity solver, must match the input field (observed)  $\rho_{\text{obs}}(\mathbf{x})$ . We quantify the mismatch using a weighted statistic  $\chi_{\omega}^2$ ,

$$\chi_{\omega}^2 = \sum_{\mathbf{x}} \frac{[\rho_{\text{mod}}(\mathbf{x}) - \rho_{\text{obs}}(\mathbf{x})]^2 \omega(\mathbf{x})}{2\sigma_{\text{obs}}^2(\mathbf{x})}, \quad (5)$$

where  $\sigma_{\text{obs}}(\mathbf{x})$  represents the observational uncertainty and  $\omega(\mathbf{x})$  is a survey window function.

Assuming a Gaussian likelihood  $\mathcal{L} \propto \exp(-\chi^2_\omega)$ , the posterior distribution for the initial field given the data is:

$$\begin{aligned} Q(\delta(\mathbf{k}) | \rho_{\text{obs}}(\mathbf{x})) &= e^{-\chi^2_\omega} \times P[\delta(\mathbf{k})] \\ &= e^{-\sum_{\mathbf{x}} [\rho_{\text{mod}}(\mathbf{x}) - \rho_{\text{obs}}(\mathbf{x})]^2 \omega(\mathbf{x}) / 2\sigma_{\text{obs}}^2(\mathbf{x})} \\ &\quad \times \prod_{\mathbf{k}}^{\text{half}} \prod_{j=0}^1 \frac{\exp\{-[\delta_j(\mathbf{k})]^2 / P_{\text{lin}}(k)\}}{[\pi P_{\text{lin}}(k)]^{1/2}}. \end{aligned} \quad (6)$$

The reconstruction problem thus reduces to sampling from this high-dimensional posterior to find the most probable initial configuration.

### 2.2.2 Hamiltonian Monte Carlo Implementation

We employ Hamiltonian Monte Carlo (HMC) to efficiently sample the posterior distribution  $Q$ . First, we define the "potential energy" function as the negative log-posterior:

$$\begin{aligned} \psi[\delta(\mathbf{k})] &\equiv -\ln Q[\delta_j(\mathbf{k}) | \rho_{\text{obs}}(\mathbf{x})] \\ &= \sum_{\mathbf{k}}^{\text{half}} \ln [\pi P_{\text{lin}}(k)] + \sum_{\mathbf{k}}^{\text{half}} \sum_{j=0}^1 \frac{[\delta_j(\mathbf{k})]^2}{P_{\text{lin}}(k)} \\ &\quad + \sum_{\mathbf{x}} \frac{[\rho_{\text{mod}}(\mathbf{x}) - \rho_{\text{obs}}(\mathbf{x})]^2 \omega(\mathbf{x})}{2\sigma_{\text{obs}}^2(\mathbf{x})}. \end{aligned} \quad (7)$$

Building on this framework, we introduce conjugate momentum variables  $p_j(\mathbf{k})$  and auxiliary "mass" parameters  $m_j(\mathbf{k})$ , and define the Hamiltonian as

$$H[\delta, p] = \sum_{\mathbf{k}}^{\text{half}} \sum_{j=0}^1 \frac{p_j^2(\mathbf{k})}{2m_j(\mathbf{k})} + \psi[\delta(\mathbf{k})]. \quad (8)$$

The associated partition function can be factorized as

$$\exp(-H) = Q[\delta(\mathbf{k}) | \rho_{\text{obs}}(\mathbf{x})] \prod_{\mathbf{k}}^{\text{half}} \prod_{j=0}^1 \exp\left[-\frac{p_j^2(\mathbf{k})}{2m_j(\mathbf{k})}\right], \quad (9)$$

which shows that drawing samples from the joint distribution  $\exp(-H)$  and integrating out the momenta produces samples from the desired posterior  $Q$ .

### 2.2.3 Sampling Algorithm

The HMC algorithm proceeds by simulating Hamiltonian dynamics in phase space  $(\delta, p)$  with

$$\frac{d\delta_j(\mathbf{k})}{dt} = \frac{\partial H}{\partial p_j(\mathbf{k})}, \quad \frac{dp_j(\mathbf{k})}{dt} = -\frac{\partial H}{\partial \delta_j(\mathbf{k})}. \quad (10)$$

In practice, these equations are integrated numerically using a symplectic leapfrog scheme. Starting from a current state  $[\delta_j(\mathbf{k}), p_j(\mathbf{k})]$ , a trajectory of length  $\tau$  (defined by the number of leapfrog steps and step size) yields a proposed new state  $[\delta'_j(\mathbf{k}), p'_j(\mathbf{k})]$ . The proposal is accepted with probability:

$$P_{\text{accept}} = \min\left\{1, \exp\left(-[H(\delta'_j(\mathbf{k}), p'_j(\mathbf{k})) - H(\delta_j(\mathbf{k}), p_j(\mathbf{k}))]\right)\right\}. \quad (11)$$

By repeating this "Hamiltonian trajectory + Metropolis update" cycle, the Markov chain explores the posterior distribution. After iterating for a sufficiently large number of steps  $N_{\text{steps}}$ , once the  $\chi^2_\omega$  value has converged, the resulting initial density field  $\delta_j(\mathbf{k})$  is taken as the final output.

## 2.3 Particle-Mesh Gravity Solvers

Our reconstruction code integrates two distinct particle-mesh (PM)  $N$ -body evolution schemes as forward models within the HMC sampler. The choice between them allows users to balance computational speed against required accuracy for specific applications.

### 2.3.1 Traditional Kick-Drift-Kick (KDK) Scheme

The first option is a conventional second-order kick-drift-kick (KDK) leapfrog integrator, which advances particle positions  $\mathbf{r}$  and velocities  $\mathbf{v}$  (in comoving coordinates) via:

$$\mathbf{v}(\mathbf{q}, a_{n+1/2}) = \mathbf{v}(\mathbf{q}, a_{n-1/2}) - \nabla \Phi(\mathbf{r}(\mathbf{q}, a_n)) \int_{a_{n-1/2}}^{a_{n+1/2}} \frac{4\pi G \bar{\rho}_0}{a \dot{a}} da, \quad (12)$$

$$\mathbf{r}(\mathbf{q}, a_{n+1}) = \mathbf{r}(\mathbf{q}, a_n) + \mathbf{v}(\mathbf{q}, a_{n+1/2}) \int_{a_n}^{a_{n+1}} \frac{1}{a^2 \dot{a}} da, \quad (13)$$

where  $\mathbf{q}$  denotes the Lagrangian coordinate,  $\Phi$  is the gravitational potential computed on the mesh,  $\bar{\rho}_0$  is the mean matter density today, and  $a$  is the scale factor with  $\dot{a} = da/dt$ .  $n$  is the step number and  $a_{n+1/2} = (a_n + a_{n+1})/2$ .

For the sake of clarity, we rewrite these equations in a form that separates the cosmology-dependent integration factors from the instantaneous dynamical terms. Using the Friedmann equation  $\dot{a} = aH(a) = aH_0E(a)$ , we define dimensionless integration factors for a step from  $a_0$  to  $a_1$ :

$$\mathcal{D}_{\text{pm}}(a_0, a_1) \equiv \int_{a_0}^{a_1} \frac{1}{a^3 E(a)} da, \quad (14)$$

$$\mathcal{K}_{\text{pm}}(a_0, a_1) \equiv \int_{a_0}^{a_1} \frac{1}{a^2 E(a)} da. \quad (15)$$

The KDK update equations can then be expressed compactly as:

$$\mathbf{v}(\mathbf{q}, a_{n+1/2}) = \mathbf{v}(\mathbf{q}, a_{n-1/2}) + \mathbf{F}_n(\mathbf{r}_n(\mathbf{q})) \mathcal{K}_{\text{pm}}(a_{n-1/2}, a_{n+1/2}), \quad (16)$$

$$\mathbf{r}(\mathbf{q}, a_{n+1}) = \mathbf{r}(\mathbf{q}, a_n) + \mathbf{P}_{n+1/2}(\mathbf{v}_{n+1/2}(\mathbf{q})) \mathcal{D}_{\text{pm}}(a_n, a_{n+1}), \quad (17)$$

where

$$\mathbf{F}_n(\mathbf{r}_n(\mathbf{q})) \equiv -\nabla \Phi(\mathbf{r}_n(\mathbf{q})) \times \frac{4\pi G \bar{\rho}_0}{H_0}, \quad (18)$$

$$\mathbf{P}_n(\mathbf{v}_n(\mathbf{q})) \equiv \mathbf{v}_n(\mathbf{q}) \times H_0. \quad (19)$$

Here,  $\mathbf{F}_n$  is the scaled gravitational force and  $\mathbf{P}_{n+1/2}$  is the scaled momentum. The prefactors  $4\pi G \bar{\rho}_0 / H_0$  and  $H_0$  are absorbed into these definitions to make the factors  $\mathcal{D}_{\text{pm}}$  and  $\mathcal{K}_{\text{pm}}$  purely geometric integrals, as defined in Eqs. (14) and (15).

This scheme assumes constant force and velocity within each time step, performing alternating "kick" (velocity update) and "drift" (position update) operations.

Although it is robust and widely adopted, the KDK scheme produces larger amplitude and phase errors on large scales when using coarse time stepping, because it does not perfectly reproduce the linear growth of cosmological perturbations. Consequently, achieving high accuracy demands a comparatively large number of time steps, which raises the computational cost.

### 2.3.2 FastPM Modified-Factor Scheme

The second option implements the *FastPM* algorithm developed by Feng et al. (2016), which modifies the kick and drift factors to ensure exact linear growth on large scales even with finite time steps. This

scheme is derived from the equations of motion in the Zeldovich approximation and corrects the integration factors to match linear theory evolution exactly for the displacement and velocity fields.

The modified drift ( $\mathcal{D}_{\text{FASTPM}}$ ) and kick ( $\mathcal{K}_{\text{FASTPM}}$ ) factors are defined as:

$$\mathcal{D}_{\text{FASTPM}} = \frac{\Delta[x_{\text{ZA}}]_{a_0}^{a_1}}{p_{\text{ZA}}} = \frac{1}{a_r^3 E(a_r)} \left( \frac{\Delta[G_p]_{a_0}^{a_1}}{g_p(a_r)} \right), \quad (20)$$

$$\mathcal{K}_{\text{FASTPM}} = \frac{\Delta[p_{\text{ZA}}]_{a_0}^{a_1}}{f_{\text{ZA}}} = \frac{1}{a_r^2 E(a_r)} \left( \frac{\Delta[G_f]_{a_0}^{a_1}}{g_f(a_r)} \right), \quad (21)$$

where  $a_r$  is a reference scale factor (typically the midpoint of the interval),  $E(a) \equiv H(a)/H_0$  is the dimensionless Hubble parameter, and  $D(a)$  is the linear growth factor. The auxiliary functions are:

$$g_p(a) = \frac{dD}{da}, \quad (22)$$

$$g_f(a) = \frac{d}{da} \left[ a^3 E(a) g_p(a) \right] = 3a^2 E \frac{dD}{da} + a^3 \frac{dE}{da} \frac{dD}{da} + a^3 E \frac{d^2 D}{da^2}, \quad (23)$$

$$G_p(a) = D(a), \quad G_f(a) = a^3 E(a) g_p(a). \quad (24)$$

These correction factors explicitly account for the evolution of the cosmological scale factor, guaranteeing that displacements, velocities, and forces follow the behavior predicted by linear perturbation theory on large scales, independent of the chosen time step size.

### 2.3.3 Connection to the traditional KDK factors

It is instructive to examine the behavior of these modified factors in the limit of an infinitesimal time step. When  $a_1 \rightarrow a_0$ , the definitions of the functions in Eqs. (22), (23), and (24) imply that the finite differences approach their differential forms:

$$\frac{\Delta G_p}{\Delta a} \rightarrow g_p, \quad \frac{\Delta G_f}{\Delta a} \rightarrow g_f \quad (25)$$

Combining this limit with the definitions of the traditional factors  $\mathcal{D}_{\text{pm}}$ ,  $\mathcal{K}_{\text{pm}}$  (Eqs. (14) and (15)) and the FastPM factors  $\mathcal{D}_{\text{FASTPM}}$ ,  $\mathcal{K}_{\text{FASTPM}}$  (Eqs. (20) and (21)), we obtain the convergence result stated:

$$\mathcal{D}_{\text{FASTPM}} \rightarrow \mathcal{D}_{\text{pm}}, \mathcal{K}_{\text{FASTPM}} \rightarrow \mathcal{K}_{\text{pm}}, \quad (26)$$

This demonstrates that, on an infinitesimal time step, the modified FastPM scheme converges to the usual drift and kick operators defined by the traditional KDK factors.

### 2.3.4 Comparison and Usage

The primary advantage of the FastPM scheme is its ability to achieve high accuracy—particularly on linear and quasi-linear scales—with significantly fewer time steps than the traditional KDK integrator. This translates directly to reduced computational cost per HMCMD sample, which is critical for the overall efficiency of the reconstruction pipeline. In our implementation, users can select either integrator via a configuration parameter, with FastPM recommended for most production runs due to its superior accuracy per computational expense. For very high-resolution simulations where small-scale forces dominate, the traditional KDK scheme remains a viable option, though at the cost of increased time steps to maintain comparable large-scale accuracy.

## 2.4 Accelerating Convergence: An Initial Density Field Guess Module

One of the main computational burdens of HMCMD-based reconstruction stems from the lengthy “burn-in” period required for the Markov Chain to transition from an arbitrary initial state into the high-probability region of the posterior distribution. To mitigate this, we introduce a rapid, approximate method that generates an informed initial estimate of the density field. This estimate serves as a high-quality starting point for the HMCMD sampler and significantly cuts down the number of steps needed to achieve convergence.

### 2.4.1 Motivation and

As shown in the right panel of Figure 1, the standard method begins the chain from a random Gaussian field sampled from the prior power spectrum  $P_{\text{lin}}(k)$ . While this initialization is statistically valid, it typically lies far from the desired posterior mode, so the chain often requires hundreds to thousands of costly forward simulations before it reaches an efficient sampling regime.

Our new module introduces an alternative route for initialization: it quickly generates a physically plausible estimate  $\delta_{\text{guess}}(\mathbf{k})$  that already closely matches the true initial conditions. This estimate is then adopted as the initial state  $\delta_i^{(0)}$  for the HMCMD chain, thereby skipping most of the burn-in period. The module runs entirely as a pre-processing step and adds only negligible overhead to the overall pipeline.

### 2.4.2 Algorithm: Approximate Linear Inversion

The guess of the initial density field is generated through an approximate linear inversion of the input final density field  $\rho_p(\mathbf{x})$ , inspired by the same transfer-function correction used in the forward model (Section 2.1). The procedure is as follows:

- **Compute the relative change kernel**

Using simulated data at both an initial and a final redshift, we define a scale-dependent amplitude transfer function in Fourier space:

$$T_{\text{guess}}(k) = \sqrt{\frac{D(z)^2 P_k(z=0, k)}{P_k(z=z_{\text{ini}}, k)}}, \quad (27)$$

where  $P_k(z, k)$  represents the power spectrum measured from the reference simulation. In principle, a high-accuracy estimate of this function should be obtained from an accuracy simulation. However, running an accuracy simulation solely for this kernel is computationally prohibitive, especially when preparing for large-scale reconstructions. To conserve substantial resources, we instead compute this function using the **CSST Emulator**, which provides a fast and acceptably accurate approximation for the corresponding cosmology (see Appendix B).

- **Apply approximate inversion:**

The input field  $\rho_{\text{obs}}(\mathbf{x})$  is first smoothed with a kernel  $R_{\text{sml}}$  and corrected for the CIC assignment window  $W_{\text{cic}}$  with given number of Meshes. It is then inversely weighted by  $T_{\text{guess}}(k)$  to approximately “rewind” gravitational growth:

$$\delta_{\text{guess}}(\mathbf{k}) = \frac{\tilde{\rho}_p(\mathbf{k})}{T_{\text{guess}}(k) R_{\text{sml}}(k) W_{\text{cic}}(k)}. \quad (28)$$

Here  $\tilde{\rho}_{\text{obs}}(\mathbf{k})$  is the Fourier transform of the pre-processed observed field on grids. The product  $R_{\text{sml}} W_{\text{cic}}$  constitutes the combined kernels mentioned above.

- **Output:**

The resulting field  $\delta_{\text{guess}}(\mathbf{k})$  is transformed back to real space and serves as the proposed guess of the initial density field.

#### 2.4.3 Advantages

The guess field  $\delta_{\text{guess}}$  is *not* intended as a standalone reconstruction. It neglects mode coupling, non-Gaussianities induced by non-linear evolution, and posterior uncertainties. Consequently, its accuracy is limited, particularly on small scales where non-linear effects are strong.

However, its primary advantage is that it delivers a *physically informed initial estimate* that is already correlated with the true starting conditions. When used to initialize the HMCMC chain,  $\delta_{\text{guess}}$  generally falls within the attraction basin of the posterior mode, allowing the sampler to reach equilibrium orders of magnitude more quickly than when starting from a random state. As shown in Section 3.5, this leads to substantial reductions in CPU time, particularly for large-volume reconstructions where burn-in would otherwise require several hundred forward simulation steps.

This module represents a classic trade-off: a small upfront investment in fast, approximate preprocessing yields disproportionately large gains in the efficiency of subsequent high-fidelity, but expensive, Bayesian sampling.

### 3 RECONSTRUCTION PERFORMANCE:

We evaluate the performance of our MPI-parallelized reconstruction code using a series of tests carried out on the Siyuan computing cluster. Our assessment targets three main aspects: (1) computational scalability with respect to both the reconstruction size and the number of processors, (2) memory usage efficiency, (3) the accuracy of the reconstructions, and (4) the speedup provided by the new initial guess module.

#### 3.1 Simulations used to evaluate performance

Since this study primarily aims to develop a highly efficient MPI code for initial-condition reconstruction, we directly utilize the density field from pre-existing N-body simulations. The final density fields used as inputs for the reconstruction are taken from cosmological  $N$ -body simulations, under the assumption of a spatially flat  $\Lambda$ CDM cosmology. To ensure robustness, we employ three independent sets of simulations:

- **Gadget-4 Simulations**

For this work, we run a set of cosmological simulations using GADGET-4 (Springel et al. 2022) by ourselves, with the cosmological parameters  $\Omega_{m,0} = 0.3111$ ,  $\Omega_{\Lambda,0} = 0.6889$ ,  $h = 0.6766$ , and  $\sigma_8 = 0.8159$ . The initial linear power spectra for these simulations are generated using CLASS (Blas et al. 2011).

- **Kun Simulations**

The second group of simulations comes from the Kun simulation project (Chen et al. 2025), which is part of the Jutian simulation suite ((Han et al. 2025)). For consistency, the fiducial run adopts the same  $\Lambda$ CDM cosmological parameters as described above.

- **Quijote Simulations**

We also utilize data from the QUIJOTE simulation suite (Villaescusa-Navarro et al. 2020) for low-resolution accuracy tests, ensuring that our results are not specific to a single simulation code.

To investigate performance on different scales, we use simulation boxes of size  $L_{\text{box}} = 1000 h^{-1} \text{Mpc}$  with varying particle counts:  $256^3$ ,  $512^3$ , and  $1024^3$ . All simulations share a common redshift starting point of  $z_{\text{ini}} = 127$ . The corresponding final density fields at  $z = 0$  serve as the observational targets  $\rho_{\text{obs}}$  in our reconstruction tests, whereas the true initial conditions are stored for subsequent accuracy validation.

#### 3.2 Scaling Performance

To evaluate the parallel efficiency and computational complexity of our MPI implementation, we conduct two complementary types of scaling tests.

- **Processor-number scaling** evaluates how the wall-clock time decreases as the number of MPI processes ( $N_{\text{proc}}$ ) increases, while the total number of particles (or grids) remains constant. This probes how efficiently the code parallelizes for a fixed problem size.

- **Particle-number scaling** (at fixed parallelism) evaluates how the wall-clock time grows with increasing total particle numbers when the number of MPI processes is kept fixed. This reflects the computational complexity of the algorithm for a given parallel setup and is essential to predict the cost of larger-scale simulations.

We conduct experiments with three problem sizes containing  $256^3$ ,  $512^3$ , and  $1024^3$  particles. For the  $256^3$  and  $512^3$  configurations, we employ  $N_{\text{proc}} = 64, 128, 256, 512$ , and  $1024$ . For the largest configuration,  $1024^3$ , we extend the scaling study to higher parallelism with  $N_{\text{proc}} = 256, 512, 1024$ , and  $2048$ . The lower bound of  $N_{\text{proc}} = 256$  is imposed because simulations with fewer processes would require excessive runtime for repeated benchmarks. All reported timings correspond to the wall-clock time required for ten full HMCMC iterations (each consisting of one forward simulation and one Hamiltonian update). The outcomes are presented in Figure 2.

##### 3.2.1 Processor-number scaling

The left panel of Figure 2 presents the Processor-number scaling performance. To compare the scaling trends of different particle numbers on a unified plot, we normalize the runtime for each to a common reference point on the ideal scaling line (dashed).

The  $256^3$  and  $512^3$  particle runs are normalized by their runtime at  $N_{\text{proc}} = 64$ , which serves as the anchor point (normalized time = 1 at  $N_{\text{proc}} = 64$ ).

For the  $1024^3$  particle runs, we also wish to anchor them to the same ideal line starting at  $N_{\text{proc}} = 64$ . However, our smallest process count for the  $1024^3$  case is  $N_{\text{proc}} = 256$ . Therefore, we first normalize the  $1024^3$  particle runtime by its value at  $N_{\text{proc}} = 256$ . Then, to correctly place this starting point on the ideal line relative to the  $N_{\text{proc}} = 64$  anchor, we apply a correction. Since increasing from 64 to 256 processes (a factor of 4) under ideal strong scaling would reduce the runtime by a factor of 4, we divide the normalized  $1024^3$  time series by the same factor of 4. This operation effectively projects its performance trend onto the same reference ideal scaling line as the smaller problem sizes, allowing a direct visual comparison of how parallel efficiency degrades with increasing  $N_{\text{proc}}$  across different particle numbers.

All test cases exhibit a substantial speed-up as  $N_{\text{proc}}$  increases, even though the scaling efficiency steadily decreases. This departure

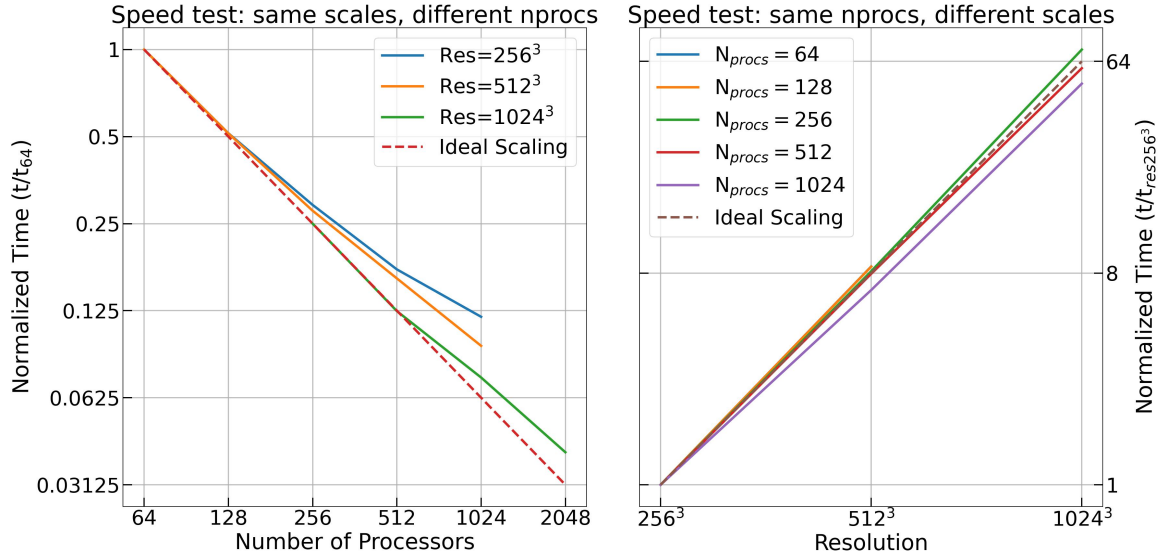


**Figure 2.** Parallel scaling performance. **(Left)** **Processor-number scaling** for fixed particle numbers ( $256^3$ ,  $512^3$ ,  $1024^3$  particles). Runtime per iteration is normalized to show parallel efficiency relative to ideal linear scaling (dashed line). Larger problems scale better. **(Right)** **Particle-number scaling** at fixed MPI process counts. Runtime scales nearly linearly with total particle count (dashed line). The flatter slopes for higher process counts originate from load imbalance at the smallest problem size used for normalization (see Section 3.2).

from ideal scaling is anticipated and can be ascribed to two primary factors:

- **Communication overhead:** As  $N_{proc}$  grows, the relative cost of MPI communication (for particle passing, force synchronization, and Fourier transforms) increases compared to local computation.
- **Load imbalance:** Our domain decomposition divides the simulation volume into spatial subdomains. As the number of these subdomains grows, statistical fluctuations in the number of particles per subdomain become more significant, which in turn increases the imbalance of computational workload across processes.

However, as the number of particles increases, the loss in efficiency becomes smaller. The  $512^3$  case exhibits better scaling efficiency—its curve stays nearer to the ideal line—than the  $256^3$  case. This is because a larger problem size results in more computation per process for a fixed  $N_{proc}$ , which more effectively spreads out the cost of the constant communication and synchronization overhead.

Importantly, this pattern persists for the even larger  $1024^3$  case. Although its normalized values are shifted because of the different normalization reference (as discussed above), the slope of its curve—reflecting how quickly efficiency is lost as  $N_{proc}$  grows—is the most favorable of the three. Among all cases, the  $1024^3$  curve deviates the least from ideal scaling as  $N_{proc}$  increases from 256 to 2048. This strongly indicates that our parallel implementation becomes progressively more efficient for the large problem sizes that are the main focus of this work, as the computation-to-communication ratio improves.

### 3.2.2 Particle-number scaling

The right panel of Figure 2 examines how computational cost grows with the total number of particles while keeping the parallel resources fixed at a given value of  $N_{proc}$ . For each chosen process count (e.g., 64, 128, 256, 512), we record the wall-clock time per iteration as the total number of particles is increased from  $256^3$  up to  $1024^3$ .

The results indicate that, for each fixed value of  $N_{proc}$ , the runtime grows roughly linearly with the total number of particles, as evidenced by the curves largely tracking the ideal dashed line. Such linear behavior is anticipated because the main computational kernels exhibit a time complexity that is nearly  $O(N)$  with respect to the particle or grid count over the range investigated.

An important pattern to note is that the slopes of these curves decrease as  $N_{proc}$  grows (for example, the blue curve for  $N_{proc} = 64$  has a steeper slope than the purple curve for  $N_{proc} = 1024$ ). This behavior arises directly from the load imbalance effect described in the Processor-number scaling analysis.

Specifically, for the smallest problem size ( $256^3$ ), using a large  $N_{proc}$  leads to significant load imbalance. Each process holds only a few particles, so random fluctuations in particle counts across subdomains become large compared to the average. Consequently, the observed runtime for the  $256^3$  case is longer than it would be with ideal load balance. Because this  $256^3$  runtime is used as the normalization baseline for each  $N_{proc}$  curve, the overestimated reference makes the normalized runtimes of the larger problems ( $512^3$  and  $1024^3$ ) look artificially small—producing the apparent flattening of the slope.

Put differently, the downward trend in the curve does not indicate that the algorithm becomes more efficient at large  $N_{proc}$ . Instead, it reflects the growing penalty of load imbalance in the small-scale reference configuration. While this skews the normalized representation, the unnormalized timing data still show the expected, nearly linear increase with problem size. Crucially, in the large production runs (e.g.,  $1024^3$  at high  $N_{proc}$ ), the effect of load imbalance is reduced because each process handles a sufficiently large, statistically representative particle sample, resulting in more stable and efficient scaling.

In conclusion, the MPI-parallel implementation delivers strong and scalable performance suitable for large-volume reconstructions. It maintains good strong-scaling behavior up to at least 1024 processes for medium-sized problems ( $512^3$ ) and achieves efficient scal-

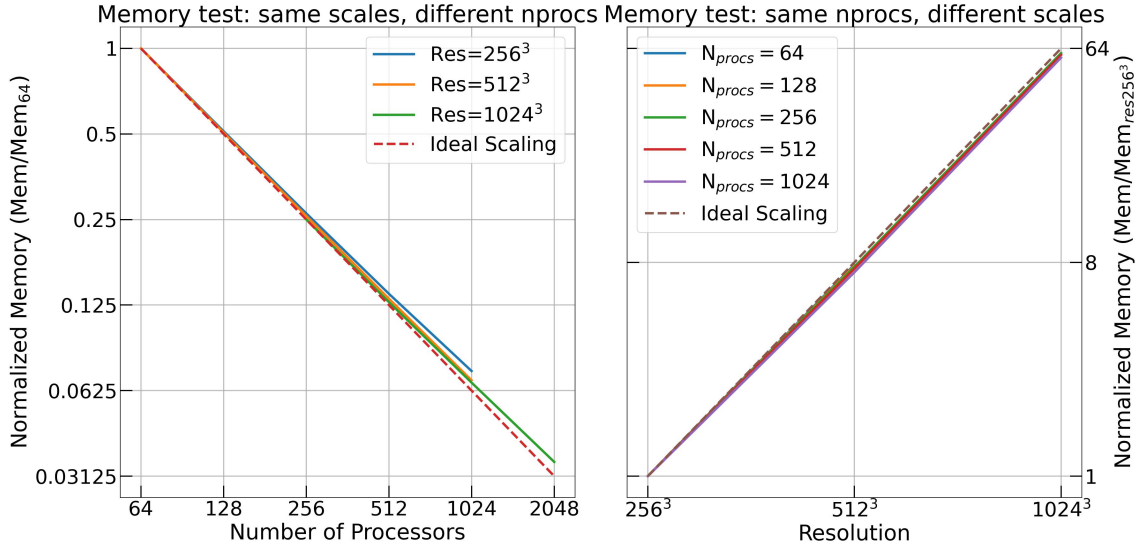


**Figure 3.** Memory usage per MPI process. **(Left)** **Processor-number scaling:** Memory per process for fixed reconstruction particle numbers ( $256^3$ ,  $512^3$ ,  $1024^3$ ), normalized to show efficient reduction relative to ideal scaling (dashed line). **(Right)** **Particle-number scaling:** Memory per process as a function of total particle count, with the number of MPI processes held constant for each curve. All curves exhibit highly linear scaling, closely following the ideal dashed line, confirming predictable memory requirements essential for large-scale initial condition reconstruction (see Section 3.3).

ing up to 2048 processes for the large problem ( $1024^3$ ). Although parallel efficiency inevitably drops at very high process counts for a fixed small problem due to communication overheads and load imbalance, performance on large problem sizes—the central focus of this work—remains excellent. The nearly linear dependence of runtime on problem size at fixed parallel resources ensures predictable computational costs for even larger simulations. Collectively, these scaling characteristics satisfy and even surpass the demands of performing full Bayesian reconstructions of initial conditions for next-generation galaxy surveys within realistic computational budgets.

### 3.3 Memory Usage

In large-scale cosmological reconstructions, available memory typically sets the upper limit on the number of particles that can be used. Moving from a shared-memory (OpenMP) setup to a distributed-memory (MPI) framework is intended precisely to mitigate this limitation by distributing the global state over multiple compute nodes. In this section, we assess the memory efficiency of our implementation.

Figure 3 shows the memory consumption per MPI process for the test setups described in Section 3.2. The left panel reports strong-scaling memory efficiency: for a fixed global problem size ( $256^3$ ,  $512^3$ , and  $1024^3$ ), the memory used by each process decreases almost ideally as the number of processes is increased. The tight overlap of the curves indicates that this behavior is essentially independent of the overall problem size.

The right panel plots memory per process against total problem size at fixed numbers of MPI processes. For any given  $N_{\text{proc}}$ , the memory per process grows linearly with the total number of particles. This is demonstrated by the curves for different  $N_{\text{proc}}$  nearly coinciding and following closely the ideal dashed line, which indicates perfect linear scaling extrapolated from the  $256^3$  reference. The excellent agreement shows that our domain decomposition strategy incurs negligible overhead and that the memory cost associated with a given subvolume is highly predictable.

A small but systematic feature is that all measured curves fall

slightly below the ideal line. This weak departure from perfect linearity is most likely caused by the amortization of fixed or slowly growing overheads—such as allocator metadata, communication buffer bookkeeping, or auxiliary data structures—whose relative impact decreases as the per-process workload grows.

This near-perfect linear and predictable scaling is critical for planning future massive reconstruction runs. It enables robust extrapolation of memory demands to substantially larger problems, ensuring that simulations with up to  $8192^3$  particles or more can be scheduled with confidence within the available memory budgets of contemporary high-performance computing systems.

#### 3.3.1 Practical Implications for ELUCID-DESI Reconstruction

The nearly linear and highly predictable scaling behavior enables us to extrapolate memory needs to larger problem sizes with substantial confidence. We are currently preparing for ELUCID-DESI runs with approximately  $8192^3$  particles. Our measurements indicate that a reconstruction with  $8192^3$  particles distributed over 32768 MPI processors on 512 nodes would require on the order of 400 GB of memory per node. This projected usage comfortably fits within the capabilities of current high-performance computing nodes. As a concrete example, the Siyuan cluster offers 512 GB of RAM per node, so a run of this scale would consume roughly 80% of the available memory, still leaving adequate margin for the operating system, communication buffers, and I/O overhead.

Consequently, the MPI-based parallelization removes the memory bottleneck that would otherwise make such a large reconstruction infeasible in the original shared-memory (OpenMP) implementation. In combination with the computational scaling behavior discussed in Section 3.2, this demonstrates that our code can carry out Bayesian reconstructions at the scales required by our upcoming ELUCID-DESI reconstruction, while maintaining predictable, controllable resource demands and thereby ensuring robustness and practicality in real computing environments.

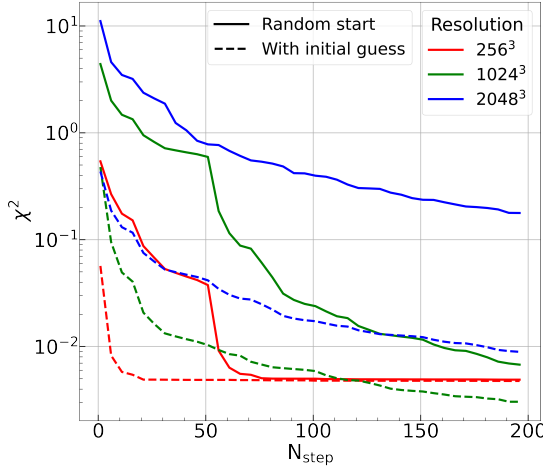


**Figure 4.**  $\chi^2_\omega$  values as a function of the number of steps  $N$ . Results are shown for chains started from a random field (solid curves) and from the guess module (dashed curves) for three problem sizes ( $256^3$ ,  $1024^3$ ,  $2048^3$ ). In all cases, the guess module delivers a better initial condition (lower starting  $\chi^2_\omega$ ) and yields faster convergence. This speed-up becomes increasingly significant as the problem size grows.

### 3.4 Reconstruction Accuracy

After examining the computational performance of our MPI-parallelized code, we next focus on its reconstruction accuracy. We assess this accuracy at both low ( $256^3$ ) and high ( $1024^3$ ) resolutions by comparing the reconstructed initial fields to the known true initial conditions from simulations. For the low-resolution tests, we use data from GADGET-4 and the QUIJOTE simulation suite (Villaescusa-Navarro et al. 2020), whereas the high-resolution test relies on a simulation from the Kun suite (Chen et al. 2025).

#### 3.4.1 Low-Resolution Tests ( $256^3$ )

We begin by validating the core functionality and convergence of the code at a manageable resolution of  $256^3$  particles, using the parameters  $N_{\text{pmstep}} = 10$ ,  $R_{\text{pm}} = 0.75$ , and  $R_s = 3.0$ . Under these settings, we run the HMC sampler for 200 iterations on a  $256^3$  density field.

Convergence is assessed through the evolution of the  $\chi^2_\omega$  statistic (Equation 5). As indicated by the red solid curve in Figure 4 (corresponding to a run initialized from a random field),  $\chi^2_\omega$  rapidly decreases from an initial value of 0.54 to below 0.01 within the first 55 iterations, and settles to a stable value of  $\sim 0.005$  by iteration 80. This trend demonstrates that the HMC sampler quickly reaches the high-probability region of the posterior.

A detailed visual and quantitative evaluation of the reconstruction performance is provided in Figure 5. The top row shows two-dimensional projections of the 3D density fields, obtained by integrating along one Cartesian axis. The left and middle panels display the true and reconstructed initial density fields, respectively, illustrating that the underlying structure is well recovered. The top-right panel shows the relative error map, which displays no coherent large-scale patterns, indicating that the reconstruction is unbiased. The bottom row shows the corresponding final density fields at  $z = 0$ : the left panel derived from the true initial conditions and the right panel from evolving the reconstructed field. Their close similarity confirms that the forward model accurately reproduces the target distribution.

We further characterize the reconstruction accuracy with the phase correlation of the Fourier phases between the true and reconstructed initial fields,  $C_p(k)$ , shown in the bottom-right panel. The correlation is unity on large scales and decreases towards smaller scales, as anticipated. The characteristic wavenumber  $k_c$  at which  $C_p(k)$  experiences a marked decline is well captured by the empirical relation  $k_c \approx 1.88/R_s^{0.94}$  from Wang et al. (2013), indicated by the vertical dashed line. This consistency verifies that the smoothing scale  $R_s$  effectively controls the scale up to which phase information is recovered, and that our results align with previous foundational work based on OpenMP code.

#### 3.4.2 Higher-Resolution Tests ( $1024^3$ )

We next evaluate the code at a higher resolution, testing the reconstruction on a density field discretized on a  $1024^3$  grid and derived from the Kun simulation. Using parameters  $N_{\text{pmstep}} = 10$ ,  $R_{\text{pm}} = 2.0$ , and  $R_s = 5.0$ , we perform 200 HMC iterations, after which  $\chi^2_\omega$  converges to a stable value of 0.0066. The reconstructed initial conditions are then forward-evolved to  $z = 0$  using GADGET-4 for direct comparison with the original input field.

A visual inspection of the resulting density fields (Figure 6) shows that the large-scale cosmic web—voids, filaments, and clusters—is well recovered, though some mismatch in the amplitudes of the highest-density clusters persists.

To quantify the agreement, we calculate the power spectra of the original and reconstructed final fields (Figure 7, top panel). The two power spectra closely match over nearly all wavenumbers, indicating that both the overall amplitude and the scale dependence of the density fluctuations are accurately reconstructed. The lower panel presents the relative difference, which stays below 5% for  $k > 0.05 h \text{ Mpc}^{-1}$ . The larger deviations on the very largest scales (the first few  $k$ -bins) are a well-known characteristic of HMC reconstructions (Wang et al. 2013, 2014), driven by sample variance from the small number of independent modes in a finite simulation volume.

Finally, Figure 8 presents a density-density scatter plot between the original and reconstructed fields at  $z = 0$ , smoothed with a  $4.8 h^{-1} \text{ Mpc}$  Gaussian kernel. The tight correlation along the one-to-one line (solid black) and the symmetric contours encompassing 67%, 95%, and 99% of the grid cells indicate unbiased recovery of the density field. The scatter, represented by the width of the contours, quantifies the remaining uncertainty, which is expected given the approximate nature of the FastPM forward model and the finite number of MCMC samples.

#### 3.4.3 Summary

The accuracy tests confirm that our MPI-parallelized implementation successfully inherits the reconstruction precision of the original ELUCID algorithm. The code converges robustly, accurately recovers the large-scale structure and power spectrum, and produces statistically unbiased density fields. The observed limitations—smoothing of fine details and increased variance on the largest scales—are understood properties of the method and can be tuned via parameters like  $R_s$  and  $N_{\text{pmstep}}$ . These results validate the code for scientific applications on large-volume datasets.

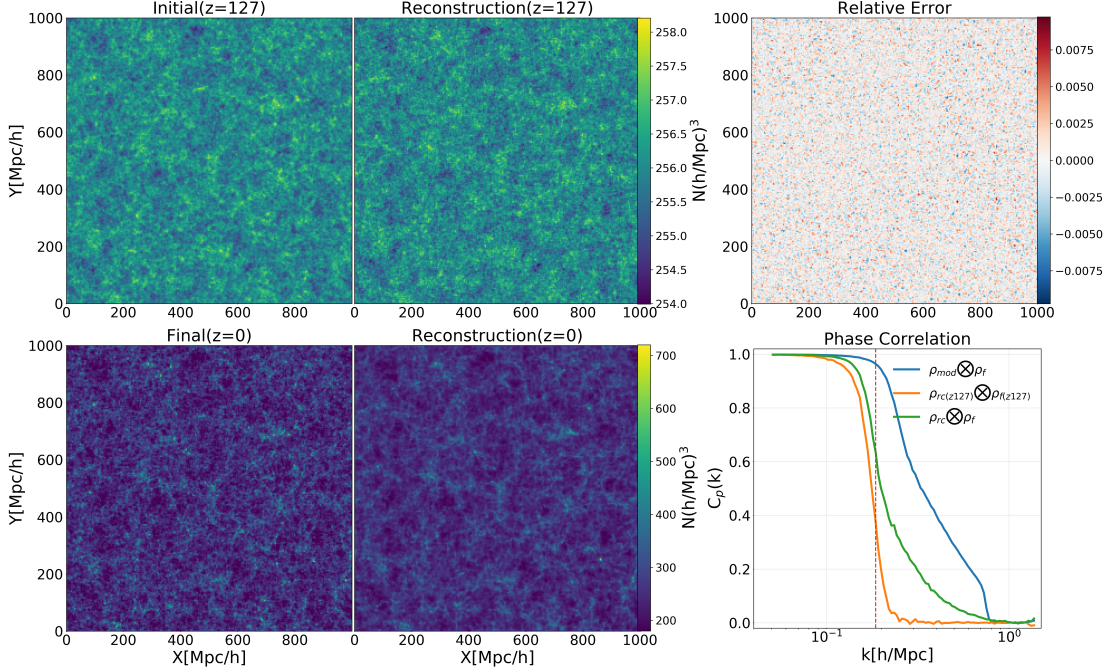


**Figure 5.** Visual and quantitative assessment of a  $256^3$  reconstruction. **Top left:** True initial density field at  $z_{\text{ini}}$ . **Top middle:** Reconstructed initial density field. **Top right:** Relative error map, showing no coherent large-scale bias. **Bottom left:** Final density field at  $z = 0$  evolved from the true initial conditions (the reconstruction target). **Middle right:** Final density field at  $z = 0$  evolved from the reconstructed initial conditions. **Bottom right:** Phase-correlation coefficient  $r(k)$  of Fourier phases. The blue line shows  $C_p(k)$  between the smoothed final field ( $\rho_{\text{mod}}$ ) and the true final field. The orange line shows  $C_p(k)$  between the reconstructed initial field and the true final field. The green line shows  $C_p(k)$  between the final field evolved from the reconstruction ( $\rho_{\text{re}}$ , after CIC assignment) and the true final field. The vertical dashed line marks the theoretical characteristic scale  $k_c \approx 1.88/R_s^{0.94}$  from Wang et al. (2013).

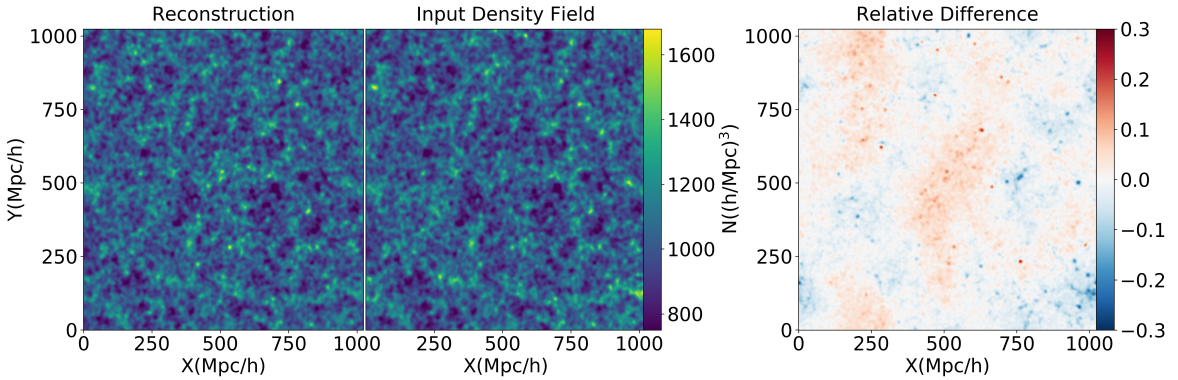


**Figure 6.** Final density fields at  $z = 0$  for the  $1024^3$  test case. **Left:** Field obtained by evolving the reconstructed initial conditions with GADGET-4. **Middle:** Original input field from the Kun simulation. **Right:** The relative error map. The overall cosmic web structure is faithfully reproduced.

### 3.5 Advantage of the Initial Guess Module

The initial guess module introduced in Section 2.4 is designed to accelerate HMC/MC convergence by providing a high-quality starting point close to the posterior mode. Here, we quantify its effectiveness by comparing reconstruction chains initialized with (i) a random Gaussian field (traditional method) and (ii) the output of our guess module.

Figure 4 shows the evolution of the  $\chi^2_\omega$  values as a function of the number of steps  $N$  for three problem sizes with  $256^3$ ,  $1024^3$ ,

and  $2048^3$  particles. In all cases, chains initialized with the guess module (dashed lines) begin with a significantly lower  $\chi^2_\omega$  than their random-initialized counterparts (solid lines). More importantly, they exhibit a steeper initial descent and reach convergence in markedly fewer iterations.

We quantify the acceleration in two ways (see Table 1):

- **Head-start advantage**

The initial  $\chi^2_\omega$  of the guess-initialized chain is equivalent to that

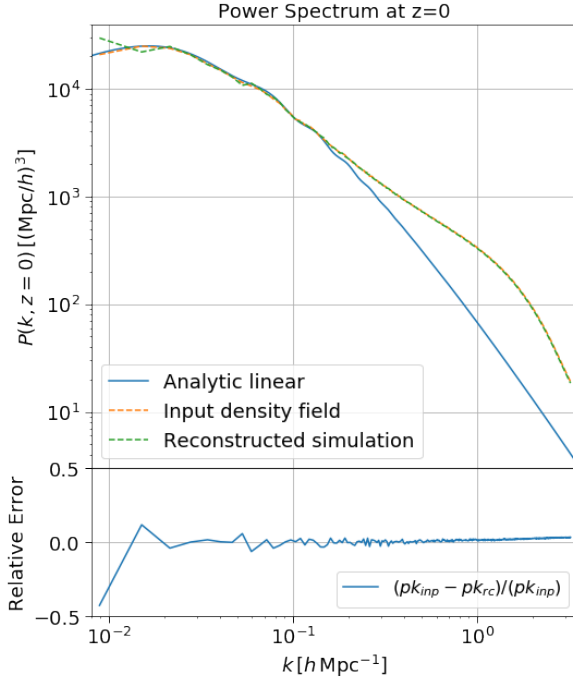


**Figure 7.** Power spectrum comparison for the  $1024^3$  reconstruction. **Top:** Power spectra of the original (yellow dashed) and reconstructed (green dashed) final density fields, with the linear theory spectrum (black solid) for reference. **Bottom:** Relative error of the reconstructed power spectrum. Agreement is excellent for  $k > 0.05 h \text{ Mpc}^{-1}$ ; the larger errors on the largest scales are consistent with previous HMC studies (Wang et al. 2013, 2014).

**Table 1.** Computational savings from the initial guess module. *Head-start* indicates how many HMC samples (and corresponding CPU hours) a random-start chain needs to reach the initial  $\chi^2_\omega$  of the guess-start chain. *Burn-in reduction* is the number of steps (and CPU hours) saved before convergence. Savings increase significantly with problem size.

Particles	Head-start (steps) (CPU hours)	Burn-in reduction (steps) (CPU hours)
$256^3$	27 (27.8)	53 (54.3)
$1024^3$	53 (3747)	106 (7494)
$2048^3$	90 (72540)	~180 (145,080)
...		
$8192^3$	~360 (18,570,240)	~720 (37,140,480)

achieved by the random-initialized chain only after a substantial number of steps (e.g., 27 steps for  $256^3$ , 53 steps for  $1024^3$  and 90 steps for  $2048^3$ ). This represents a more efficient starting point in the sampling process.

#### • Reduction in burn-in

We define the burn-in period as the number of iterations it takes for the chain's  $\chi^2_\omega$  to drop below 1% of its starting value for the first time. Under this definition, the guess-initialized chain converges substantially more rapidly. In the  $256^3$  test, it reaches convergence 53 iterations sooner than the randomly initialized chain; in the  $1024^3$  test, 106 iterations sooner.

Crucially, the *relative* advantage of the module grows as the problem size increases. This favorable scaling makes it especially useful for the large-volume reconstructions considered in this work. The module introduces only negligible computational overhead (just

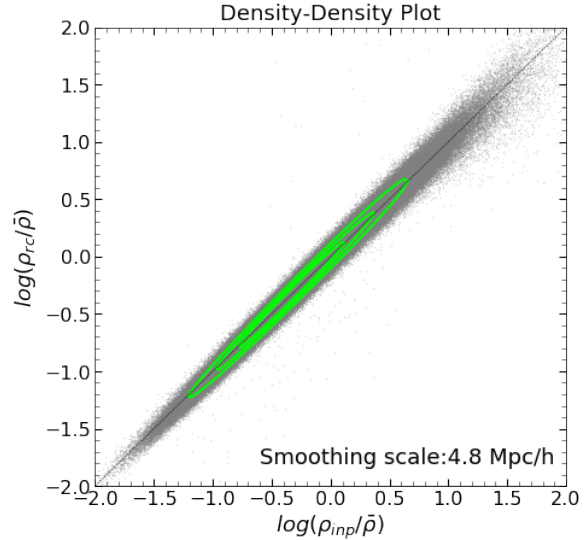


**Figure 8.** Density-density scatter plot between the original and reconstructed  $z = 0$  density fields (Gaussian smoothed with  $R = 4.8 h^{-1} \text{ Mpc}$ ). Contours enclose 68%, 95%, and 99% of grid cells. The tight correlation around the one-to-one line (solid black) indicates unbiased reconstruction.

a single, fast, approximate inversion) while delivering order-of-magnitude reductions in the cost of the subsequent, expensive HMC sampling.

These computational gains convert directly into substantial savings in CPU hours, which become striking at large problem sizes (Table 1). Extrapolating from the  $256^3$  and  $1024^3$  examples, we estimate that for a  $2048^3$  run the guess module could save roughly 145,000 CPU hours. For our planned ELUCID-DESI simulation with  $8192^3$  particles, the savings increase to about 37,000,000 CPU hours.

In conclusion, the initial guess module achieves its intended purpose: it dramatically shortens the burn-in phase of the HMC sampler, producing enormous computational savings without degrading the final reconstruction accuracy (which remains the same once the chains have converged). This, in turn, renders rigorous Bayesian reconstruction practical for future survey-scale datasets.

## 4 DISCUSSION AND CONCLUSION

In this study, aiming at performing the future ELUCID-DESI reconstruction simulations, we have introduced a significant computational advance for the Bayesian reconstruction of the initial condition of the cosmic density field. By re-implementing the HMC algorithm in a distributed-memory, MPI-parallel environment and equipping it with an intelligent initial-guess module, we overcome the two main obstacles that previously hindered its application to next-generation survey volumes: memory limitations and excessive computational expense.

The strength of our MPI implementation stems from an effective domain-decomposition strategy. Although we see the expected drop in Processor-number scaling efficiency at very high process counts, performance remains excellent for the large problem sizes that are our primary focus. The code achieves nearly strong scaling (Fig. 2), indicating that it can make efficient use of additional computational resources to handle larger volumes. This capability is vital for analyzing data from surveys such as CSST and DESI. Furthermore, the almost perfectly linear scaling of memory consumption with problem

size (Fig. 3) permits reliable extrapolation to even larger configurations, turning an 8192<sup>3</sup> reconstruction into a realistic and schedulable computational task.

The initial-guess module dramatically boosts efficiency. By shortening the HMC-MCMC burn-in phase by tens to hundreds of steps (Fig. 4, Table 1), it yields order-of-magnitude savings in total CPU time. Notably, its impact *improves* as the problem size grows, making it highly complementary to our parallelization strategy. The guess field acts as an effective “pre-conditioner” for the sampler, rapidly steering it into the high-likelihood region of the extremely high-dimensional parameter space.

Although we have addressed major scalability issues—making the method suitable for our ELUCID-DESI project—there are still several avenues for further development to support even larger data volumes or more demanding precision in reconstruction.

**Forward Model Accuracy:** For applications demanding very high accuracy on quasi-linear scales, it would be advantageous to provide a more accurate forward solver as an optional component. The modular design of our framework is intended to make such upgrades straightforward.

**Optimization for Heterogeneous Architectures:** Additional performance gains may be realized by offloading the most computationally intensive parts—the particle-mesh force calculation and FFTs—to GPUs using a hybrid MPI+OpenACC approach.

**Integration with Real Survey Data:** Applying this method to real galaxy survey data will require a careful treatment of the survey mask, redshift-space distortions, and galaxy bias modeling. For ELUCID-DESI, in a separate work we are reconstructing the DESI mass, velocity, and tidal fields using a halo-based group finder framework. Other complementary techniques, including AI-based approaches, have also been developed. (e.g., Wang et al. 2024a; Shi et al. 2025).

**Enhancing the Guess Module:** The guess module could likely be further improved by embedding a fast nonlinear approximation or a lightweight machine-learning emulator, which could reduce the burn-in period even more.

In summary, we have developed and validated a scalable, efficient computational framework that makes rigorous Bayesian reconstruction of the initial density field feasible at the scale of next-generation cosmological surveys. The core of this framework is a high-performance, MPI-parallelized implementation of the HMC-MCMC algorithm that overcomes previous memory barriers. Augmented with a novel initial guess module that dramatically reduces computational cost—with savings increasing with problem size—this tool is now poised to maximize the scientific return from missions like *Euclid*, LSST, CSST and DESI.

## ACKNOWLEDGEMENTS

This work is supported by the National Key R&D Program of China (2023YFA1607800, 2023YFA1607801, 2023YFA1607804), “the Fundamental Research Funds for the Central Universities”, 111 project No. B20019, the National Natural Science Foundation of China (Grant No. 12273088, 12595312), and Shanghai Natural Science Foundation, grant No.19ZR1466800. We acknowledge the science research grants from the China Manned Space Project with Nos. CMS-CSST-2021-A02 & CMS-CSST-2025-A04. This project is also supported in part by Office of Science and Technology, Shanghai Municipal Government (grant Nos. 24DX1400100, ZJ2023-ZD-001). HYW is supported by the New Cornerstone Science Foundation through the XPLOTER PRIZE. F.S. acknowledges the support from the State Key Laboratory of Dark Matter Physics and the Young Data

Scientist Program of the China National Astronomical Data Center (No.NADC2025YDS-01). The computations in this paper were run on the Gravity and Siyuan Supercomputer at Shanghai Jiao Tong University. Thanks to Yu Feng’s FastPM code.

## DATA AVAILABILITY

The data underlying this article will be shared on reasonable request with the corresponding author.

## REFERENCES

Bertschinger E., 1987, *ApJ*, **323**, L103  
 Blanton M. R., et al., 2005, *AJ*, **129**, 2562  
 Blas D., Lesgourgues J., Tram T., 2011, *Journal of Cosmology and Astroparticle Physics*, 2011, 034–034  
 CSST Collaboration et al., 2025, *arXiv e-prints*, p. arXiv:2507.04618  
 Chen Z., Yu Y., 2025a, Extending CSST Emulator to post-DESI era ([arXiv:2510.09503](https://arxiv.org/abs/2510.09503)), <https://arxiv.org/abs/2510.09503>  
 Chen Z., Yu Y., 2025b, *Science China Physics, Mechanics, and Astronomy*, **68**, 109513  
 Chen Z., Yu Y., Han J., Jing Y., 2025, *Science China Physics, Mechanics & Astronomy*, **68**  
 DESI Collaboration et al., 2016a, *arXiv e-prints*, p. arXiv:1611.00036  
 DESI Collaboration et al., 2016b, *arXiv e-prints*, p. arXiv:1611.00037  
 Doumler T., Hoffman Y., Courtois H., Gottlöber S., 2013, *MNRAS*, **430**, 888  
 Feng Y., Chu M.-Y., Seljak U., McDonald P., 2016, *Monthly Notices of the Royal Astronomical Society*, **463**, 2273–2286  
 Gong Y., et al., 2019, *ApJ*, **883**, 203  
 Guo Q., et al., 2011, *MNRAS*, **413**, 101  
 Hahn C., et al., 2023, *AJ*, **165**, 253  
 Han J., et al., 2025, The Jiutian simulations for the CSST extra-galactic surveys ([arXiv:2503.21368](https://arxiv.org/abs/2503.21368)), <https://arxiv.org/abs/2503.21368>  
 Hoffman Y., Ribak E., 1991, *ApJ*, **380**, L5  
 JUST Team et al., 2024, *Astronomical Techniques and Instruments*, **1**, 16  
 Jasche J., Wandelt B. D., 2013, *MNRAS*, **432**, 894  
 Jing Y. P., Mo H. J., Börner G., 1998, *ApJ*, **494**, 1  
 Kauffmann G., White S. D. M., Guiderdoni B., 1993, *MNRAS*, **264**, 201  
 Kitaura F.-S., 2013, *MNRAS*, **429**, L84  
 Kitaura F. S., Enßlin T. A., 2008, *MNRAS*, **389**, 497  
 Klypin A., Hoffman Y., Kravtsov A. V., Gottlöber S., 2003, *ApJ*, **596**, 19  
 Kravtsov A. V., Klypin A., Hoffman Y., 2002, *ApJ*, **571**, 563  
 Mo H., van den Bosch F. C., White S., 2010, *Galaxy Formation and Evolution*. Cambridge University Press, doi:10.1017/CBO9780511807244  
 Myers A. D., et al., 2023, *AJ*, **165**, 50  
 Seljak U., Aslanyan G., Feng Y., Modi C., 2017, *J. Cosmology Astropart. Phys.*, **2017**, 009  
 Shi F., et al., 2025, *ApJS*, **280**, 53  
 Sousa S. G., Santos N. C., Israelian G., Mayor M., Monteiro M. J. P. F. G., 2007, *A&A*, **469**, 783  
 Springel V., Pakmor R., Zier O., Reinecke M., 2022, GADGET-4: Parallel cosmological N-body and SPH code  
 Takada M., et al., 2014, *PASJ*, **66**, R1  
 Tweed D., Yang X., Wang H., Cui W., Zhang Y., Li S., Jing Y. P., Mo H. J., 2017, *The Astrophysical Journal*, **841**, 55  
 Villaescusa-Navarro F., et al., 2020, *ApJS*, **250**, 2  
 Wang H., Mo H. J., Jing Y. P., Guo Y., van den Bosch F. C., Yang X., 2009, *Monthly Notices of the Royal Astronomical Society*, **394**, 398–414  
 Wang H., Mo H. J., Yang X., van den Bosch F. C., 2012, *MNRAS*, **420**, 1809  
 Wang H., Mo H. J., Yang X., van den Bosch F. C., 2013, *The Astrophysical Journal*, **772**, 63  
 Wang H., Mo H. J., Yang X., Jing Y. P., Lin W. P., 2014, *The Astrophysical Journal*, **794**, 94  
 Wang H., et al., 2016, *The Astrophysical Journal*, **831**, 164  
 Wang H., et al., 2018, *The Astrophysical Journal*, **852**, 31

Wang Z., Shi F., Yang X., Li Q., Liu Y., Li X., 2024a, *Science China Physics, Mechanics, and Astronomy*, **67**, 219513

Wang Y., et al., 2024b, *ApJ*, **971**, 119

Yang X., Mo H. J., van den Bosch F. C., Jing Y. P., 2005, *MNRAS*, **356**, 1293

Yang X., Mo H. J., van den Bosch F. C., Pasquali A., Li C., Barden M., 2007, *The Astrophysical Journal*, **671**, 153–170

Yang X., Mo H. J., van den Bosch F. C., 2008, *ApJ*, **676**, 248

Yang X., Mo H. J., van den Bosch F. C., 2009, *ApJ*, **695**, 900

Yang X., Mo H. J., van den Bosch F. C., Zhang Y., Han J., 2012, *ApJ*, **752**, 41

Yang X., et al., 2018, *The Astrophysical Journal*, **860**, 30

York D. G., et al., 2000, *AJ*, **120**, 1579

Zehavi I., et al., 2005, *ApJ*, **630**, 1

Zehavi I., et al., 2011, *ApJ*, **736**, 59

Zhan H., 2011, *Scientia Sinica Physica, Mechanica & Astronomica*, **41**, 1441

Zhang Y., Yang X., Guo H., 2021, *MNRAS*, **500**, 1895

Zhang Y., Yang X., Guo H., 2022, *MNRAS*, **517**, 3579

Zhang Y., Yang X., Guo H., Wang P., Shi F., 2025, *MNRAS*, **539**, 1692

Zheng Z., et al., 2005, *ApJ*, **633**, 791

Zhou S., Chen Z., Yu Y., 2025, *Science China Physics, Mechanics, and Astronomy*, **68**, 129512

van de Weygaert R., Bertschinger E., 1996, *MNRAS*, **281**, 84

## APPENDIX A: PERFORMANCE COMPARISON WITH THE OPENMP IMPLEMENTATION

This appendix provides a detailed comparative analysis of the performance between the new MPI-parallelized reconstruction code and its original OpenMP-based counterpart. All tests were conducted on the same nodes of the Siyuan computing cluster under identical cosmological and numerical parameters (e.g.,  $N_{\text{pmstep}}$ ,  $R_s$ , particle count, and number of OpenMP threads/MPI processes equivalent to the total core count).

### A1 Observed Performance Difference

A direct, head-to-head comparison reveals a significant runtime difference: the MPI version requires approximately **7–8 times longer** to complete one HMCMD iteration (comprising ten full PM forward simulation and the Hamiltonian update) than the OpenMP version when utilizing an equivalent number of physical cores on a single node.

This slowdown is consistent across both major computational kernels: the particle-mesh (PM)  $N$ -body solver (which is dominated by 3D Fast Fourier Transforms) and the bookkeeping operations of the HMCMD sampler.

### A2 Analysis of the Performance Gap

This difference ultimately stems from the inherent architectural distinctions between the shared-memory (OpenMP) and distributed-memory (MPI) programming paradigms, which result in markedly different communication overheads.

#### • OpenMP (Shared Memory)

All threads have direct, uniform access to the entire simulation volume (density grids, particle arrays). Operations like 3D FFTs and particle force calculations can be parallelized with fine-grained loops, requiring only lightweight synchronization (e.g., atomic updates or barriers). Data movement is handled transparently by the hardware cache coherence protocol, resulting in minimal programmer-visible overhead.

#### • MPI (Distributed Memory)

The global simulation domain is partitioned into subdomains, each handled by a distinct MPI process with its own local memory. This setup introduces essential, yet expensive, communication operations:

(i) **Particle Passing:** After each drift step, particles that cross subdomain boundaries must be detected and transferred to the MPI process responsible for their new location.

(ii) **Global Transposes for 3D FFTs:** Executing a parallel 3D FFT on a distributed mesh requires several all-to-all communication phases to transpose data across dimensions, incurring latency and bandwidth overheads that grow with the number of processes.

(iii) **Force Synchronization:** Evaluating the PM force involves aggregating contributions from the distributed grid, which demands additional communication following the FFTs.

These communication steps are not present in the OpenMP implementation and form the primary source of overhead in the MPI version.

In addition, our straightforward column-based (slab) domain decomposition can introduce load imbalance because the particle count per subdomain may differ. While OpenMP’s dynamic scheduling can alleviate this, a static MPI decomposition may cause some processes to remain idle while others are still processing their particle workloads.

## A3 Conclusion and Context

The observed slowdown by a factor of roughly 8 in the MPI implementation can therefore be attributed to the inherent overhead of distributing memory and supporting simulations that surpass the memory limits of a single node. This trade-off is intentional and warranted: the OpenMP implementation is intrinsically constrained by the RAM of one machine, whereas the MPI implementation can pool memory from thousands of nodes, enabling reconstructions at scales such as 8192<sup>3</sup> particles that would otherwise be unattainable.

Consequently, the MPI implementation is not intended to replace the OpenMP version on a single node, but to serve as its essential extension for *capacity computing*—sacrificing single-node efficiency in exchange for the ability to tackle far larger problems. The substantial decrease in total wall-clock time provided by the initial guess module (Section 3.5) is key to compensating for this per-step overhead and ensuring that large-scale MPI runs remain computationally practical.

## APPENDIX B: EFFICIENT ACQUISITION OF CALIBRATION DATA

The reconstruction algorithm relies on two essential calibration data products: (1) the *correction transfer function*  $T(k)$  (Equation 1), which relates the fast PM forward model to a high-accuracy reference, and (2) the *linear-to-nonlinear power spectrum evolution curve*  $P_k(z = 0, k)/P_k(z_{\text{ini}}, k)$  employed by the initial guess module (Equation 27). The standard approach to obtain both is to perform a full-volume, high-resolution  $N$ -body simulation (for instance, with GADGET-4), but this is too computationally expensive for routine use or for scanning a wide range of cosmological parameters.

In this appendix, we introduce and assess more efficient strategies for producing these calibration data, aiming to balance accuracy against computational cost in a way that is practical for large-scale production.

## B1 Alternative Method for the Power Spectrum Evolution Curve

Instead of carrying out a full  $N$ -body simulation, we obtain the power spectrum ratio  $P(z = 0, k)/P(z_{\text{ini}}, k)$  using a **CSST Emulator**. Emulators—such as those based on the **Kun suites** (Chen et al. 2025; Chen & Yu 2025b; Zhou et al. 2025; Chen & Yu 2025a)—are trained on a grid of simulations and can deliver predictions for nonlinear power spectra at arbitrary cosmologies within the designed parameter space. In our application, the emulator-induced error is subdominant, since this curve is employed only within the initial guess module (Section 2.4). Any imperfections in the initial guess are subsequently corrected by the HMC sampling, which relies on the exact forward model and likelihood. Consequently, the emulator-based method achieves very high accuracy at negligible computational cost.

## B2 Alternative Method for the Correction Transfer Function

For the transfer function  $T(k)$ , which directly enters the likelihood evaluation at each HMC step, we adopt a **small-box, high-resolution simulation** approach. Instead of performing a reference simulation over the full survey volume (e.g.,  $L_{\text{box}} = 1000 h^{-1} \text{Mpc}$  with  $1024^3$  particles), we run a simulation with the same *mass resolution* (i.e., identical particle number density) but in a substantially smaller box (e.g.,  $L_{\text{box}} = 250 h^{-1} \text{Mpc}$ ). This “mini-simulation” reproduces the relevant nonlinear dynamics and mode coupling on small and intermediate scales ( $k > 2\pi/L_{\text{box,small}}$ ) at a significantly reduced computational cost.

The resulting  $T(k)$  is trustworthy for modes with  $k > k_{\text{min}} = 2\pi/L_{\text{box,small}}$ . On the largest scales ( $k < k_{\text{min}}$ ), one may either fall back on linear theory ( $T(k) \approx 1$ ) or extrapolate from the measured behavior. Although this approach does incur some additional error relative to a full-volume calibration, it is important to emphasize that  $T(k)$  is itself an approximate, empirically motivated correction to compensate for PM inaccuracies. The incremental uncertainty from using a small-box setup remains within the acceptable error budget of this approximation and, as our tests demonstrate, does not qualitatively compromise the final reconstruction.

## B3 Recommendation

For production applications, we recommend:

- (i) Employing an emulator to compute the evolution curve of the power spectrum for the guess module. This approach is highly accurate and effectively cost-free.
- (ii) Running a high-resolution, small-volume simulation to obtain the correction transfer function  $T(k)$ . This cuts the calibration expense by roughly one to two orders of magnitude while maintaining reconstruction fidelity on all but the very largest scales.

Together, these choices substantially reduce the practical hurdles to adopting our reconstruction code, allowing users to complete the initial setup without requiring access to extreme computational resources for calibration.